INTERNATIONAL JOURNAL FOR NUMERICAL METHODS IN FLUIDS
Int. J. Numer. Meth. Fluids 2005; **47**:1469–1487
Published online 17 December 2004 in Wiley InterScience (www.interscience.wiley.com). DOI: 10.1002/fld.822

Numerical solution of three-dimensional velocity–vorticity Navier–Stokes equations by finite difference method

D. C. Lo, K. Murugesan and D. L. Young*,†

Department of Civil Engineering and Hydrotech Research Institute, National Taiwan University, Taipei, Taiwan

SUMMARY

This paper describes the finite difference numerical procedure for solving velocity–vorticity form of the Navier–Stokes equations in three dimensions. The velocity Poisson equations are made parabolic using the false-transient technique and are solved along with the vorticity transport equations. The parabolic velocity Poisson equations are advanced in time using the alternating direction implicit (ADI) procedure and are solved along with the continuity equation for velocities, thus ensuring a divergence-free velocity field. The vorticity transport equations in conservative form are solved using the second-order accurate Adams–Bashforth central difference scheme in order to assure divergence-free vorticity field in three dimensions. The velocity and vorticity Cartesian components are discretized using a central difference scheme on a staggered grid for accuracy reasons. The application of the ADI procedure for the parabolic velocity Poisson equations along with the continuity equation results in diagonally dominant tri-diagonal matrix equations. Thus the explicit method for the vorticity equations and the tri-diagonal matrix algorithm for the Poisson equations combine to give a simplified numerical scheme for solving three-dimensional problems, which otherwise requires enormous computational effort. For three-dimensional-driven cavity flow predictions, the present method is found to be efficient and accurate for the Reynolds number range $100 \leqslant Re \leqslant 2000$. Copyright © 2004 John Wiley & Sons, Ltd.

KEY WORDS: finite difference method; ADI; TDMA; velocity–vorticity formulation; Navier–Stokes equations; staggered grid

1. INTRODUCTION

Numerical methods that are used to simulate incompressible viscous flows can be classified into three major categories, namely primitive variable (velocity–pressure) [1–5] formulation, stream function vector [6, 7] or vorticity-vector-potential [8] formulation and velocity–vorticity

*Correspondence to: D. L. Young, Department of Civil Engineering and Hydrotech Research Institute, National Taiwan University, Taipei, Taiwan.
†E-mail: dlyoung@hy.ntu.edu.tw

Contract/grant sponsor: NSC, Taiwan

Received 29 March 2003
Revised 12 August 2004
Accepted 14 October 2004

[9–16] formulation. The above formulations have been thoroughly investigated by various researchers for 2D and 3D flow problems using different numerical methods. Goda [17] simulated two- and three-dimensional cavity flows using the finite difference method. The major notion of his algorithm is to deal with only one-dimensional forms for both velocity and pressure calculations in spite of the three-dimensional equations. Elshabka and Chung [6] used the finite element method to solve the fourth-order vector partial differential equations for the solution of three-dimensional stream function vector components. Weinan and Liu [8] adopted an efficient and accurate finite difference method to calculate three-dimensional unsteady viscous incompressible flows in terms of the vorticity-vector-potential formulation on non-staggered grids. In the past couple of decades, the velocity–vorticity formulation has been investigated by many researchers using various numerical schemes such as the finite difference method [18, 19], the finite element method [9, 20] and the boundary element method (BEM) [10, 11].

The velocity–vorticity form of Navier–Stokes equations pioneered by Fasel [21] has provided an effective formulation for the solution of two-dimensional computational fluid dynamics (CFD) problems. Orlandi [22] established a numerical scheme for flow over a two-dimensional backward facing step using a block alternating direction implicit (ADI) method. Liu [23] and Napolitano and Pascazio [24] among others, used the finite difference method with a staggered grid to study three-dimensional-driven cavity flow problems. Two-dimensional velocity–vorticity formulation using the finite element method was first reported by Guevremont *et al.* [25]. They used quadratic finite elements for the velocity components and linear finite elements for the vorticity components. They also reported results for three-dimensional-driven cavity flow for $Re = 100$ and 400. Recently Wong and Baker [9] developed a parallel solution algorithm for the solution of three-dimensional incompressible Navier–Stokes equations in velocity–vorticity form using the finite element method. They used Taylor's series expansion scheme to obtain second-order accurate vorticity boundary conditions at the wall boundary. Young *et al.* [10] used the Eulerian–Lagrangian BEM (ELBEM) for the solution of two-dimensional incompressible viscous flow problems using velocity–vorticity formulation. The above method is obtained by the combination of the Eulerian–Lagrangian method and the BEM. The Poisson-type velocity equations are solved using the general boundary integral method with domain integration for the source terms and the vorticity boundary conditions are exactly determined. The vorticity transport equation is solved using the ELBEM on a transformed characteristic domain. Young *et al.* [11] also provided a combined boundary element and finite element method for the numerical solution of three-dimensional incompressible viscous flow using velocity–vorticity formulation. The use of finite difference or finite element method for three-dimensional flow problems demands large computational effort in time and in computer memory especially for solving problems of high Reynolds number flows. Continuous research is going on in the field of computational fluid dynamics to develop simplified numerical procedures for the solution of three-dimensional flow problems, so that even a personal computer could be used for dealing with high Reynolds number flow. The present work concentrates to contribute in that direction.

The numerical scheme followed to solve the three-dimensional velocity–vorticity equations using the finite difference technique can be described by the following numerical procedures:

(1) The velocity Poisson equations obtained as a result of taking curl of the vorticity definition along with the continuity equation are made parabolic using the false-transient technique [18, 24, 26, 27] and hence they are accurately solved only at steady state.

(2) The velocity Poisson equations are integrated in the time domain using a scalar ADI procedure, which reduces the equations to a diagonally dominant tri-diagonal matrix. Hence a simple tri-diagonal matrix algorithm (TDMA) can be used to solve the equations for velocities.
(3) Procedure (2) is used to obtain velocities u and v in the x and y directions respectively. The velocity w in the z direction is obtained from the differentiated form of the continuity equation, thus assuring a divergence-free velocity field.
(4) The Adams–Bashforth method, which is explicit and second-order accurate in time, is used to discretize the vorticity transport equations in time. The conservative form of the vorticity transport equations are used in order to satisfy the divergence-free constraint for the vorticity field in three dimensions.
(5) The velocity and the vorticity variables in the Cartesian co-ordinates are discretized in space using a second-order accurate central difference scheme on an MAC staggered grid. The use of a staggered grid also ensures the accurate predictions of the field variables.
(6) The use of the TDMA algorithm for the velocity Poisson equations and an explicit time marching scheme for the vorticity transport equations have enabled us to use the Gauss elimination technique for the solution of the field variables.
(7) The above-simplified numerical solution procedure for the coupled governing equations has allowed us to employ a uniform mesh of size $101 \times 101 \times 101$ for obtaining the flow field for $Re = 2000$ using a Pentium-IV personal computer.
(8) As far as the vorticity boundary conditions at the wall are concerned, a second-order accurate central difference scheme is adopted to calculate the vorticity from its definition.

The contents of the paper are organized as follows: Section 2 presents the vorticity transport equations and the velocity Poisson equations. Section 3 gives the details about the finite difference numerical procedure for the solution of the governing equations in velocity–vorticity form. The numerical results for a lid-driven cubical cavity flow for $Re = 100$, 400, 1000 and 2000 are discussed in Section 4. The accuracy of the results predicted by the present numerical scheme are verified and compared with the results of other numerical schemes. Section 5 contains our main conclusions.

2. GOVERNING EQUATIONS

The partial differential equations governing the viscous, laminar flow of an incompressible fluid are given by the Navier–Stokes equations. The corresponding non-dimensional form of the governing equations for conservation of mass and momentum can be expressed in vector form as [28]:
Continuity equation

$$\nabla \cdot \mathbf{u} = 0 \tag{1}$$

Momentum equation

$$\frac{\partial \mathbf{u}}{\partial t} + \mathbf{u} \cdot \nabla \mathbf{u} = -\nabla p + \frac{1}{Re} \nabla^2 \mathbf{u} \tag{2}$$

where $\mathbf{u}$ is the velocity vector of the flow field, p is the pressure, $Re = uL/\upsilon$ is the Reynolds number and t is the time. Equations (1) and (2) represent the Navier–Stokes equations in the primitive variable (pressure–velocity) form.

By using the curl operator to Equation (2), one gets the following dimensionless form of the vorticity transport equation:

$$\frac{\partial \boldsymbol{\omega}}{\partial t} + \mathbf{u} \cdot \nabla \boldsymbol{\omega} = \boldsymbol{\omega} \cdot \nabla \mathbf{u} + \frac{1}{Re} \nabla^2 \boldsymbol{\omega} \tag{3}$$

where the vorticity vector $\boldsymbol{\omega}$ is defined as

$$\boldsymbol{\omega} = \nabla \times \mathbf{u} \tag{4}$$

By taking the curl of Equation (4) and using the continuity equation (1), the following velocity Poisson equation can be obtained:

$$\nabla^2 \mathbf{u} = -\nabla \times \boldsymbol{\omega} \tag{5}$$

Equations (3) and (5) are the velocity–vorticity form of the Navier–Stokes equations, with three equations for the velocity vector, $\mathbf{u} = (u, v, w)$ and three equations for the vorticity vector, $\boldsymbol{\omega} = (\xi, \eta, \varsigma)$ in the Cartesian co-ordinates.

We seek a solution for the field variables in the domain Ω, which satisfies the initial conditions,

$$u = u_0, v = v_0, w = w_0 \text{ at } t = 0 \tag{6}$$

and non-slip boundary conditions of velocity on the solid boundary Γ of Ω. The boundary condition for Equation (3) is obtained by using the vorticity definition of Equation (4) on the boundary.

3. FINITE DIFFERENCE NUMERICAL SCHEME

The solenoidality constraint on the vorticity field in three-dimension requires a solution of the system of governing equations represented by Equations (3) and (5) with boundary conditions given by Equations (4) and (6). However, the computation of the six field variables in a 3D domain using a direct solver is an arduous challenge. The solution of the time-dependent vorticity transport equations (3) and the elliptic Poisson equations (5) necessarily demands the use of a direct solver. The solution procedure can be simplified by making the velocity Poisson equations (5) also parabolic. This can be achieved by making use of the false-transient method proposed by Mallinson and Davis [26]. With this modification, the parabolic form of the velocity Poisson equations (5) can be expressed as

$$\alpha \frac{\partial \mathbf{u}}{\partial t} - \nabla^2 \mathbf{u} - \nabla \times \boldsymbol{\omega} = 0 \tag{7}$$

where α is a relaxation parameter. It is obvious that the steady state solutions for the flow field are obtained when the time derivatives in Equations (3) and (7) approach zero. A simple ADI algorithm can be adopted to discretize the time derivatives in Equation (7). Considering

the first component of the kinematic relations (7), it can be rewritten as a tri-diagonal system of equations of the form

$$a_i u_{i-1,j,k} + b_i u_{i,j,k} + c_i u_{i+1,j,k} = d_i \tag{8}$$

where

$$a_i = -\frac{\Delta t}{\alpha \Delta x^2}$$

$$b_i = 1 + \frac{2\Delta t}{\alpha \Delta x^2}$$

$$c_i = -\frac{\Delta t}{\alpha \Delta x^2}$$

$$d_i = R(u_{i,j,k})$$

and $R(u_{i,j,k})$ is the residual of the discretized form of the parabolic equation (7) [12]. This procedure yields $N_j \times N_k$ linear system of equations of the type given by Equation (8). Initially the velocities u and v are calculated by adopting the ADI procedure and then the velocity w is calculated from the continuity equation as given below:

$$\frac{\partial^2 w}{\partial z^2} = -\frac{\partial}{\partial z}\left(\frac{\partial u}{\partial x} + \frac{\partial v}{\partial y}\right) \tag{9}$$

Since the velocities u and v are already known the resulting set of equations from Equation (9) can be solved using the TDMA. The main advantage of the present numerical solution procedure is that it assures a divergence-free solution for the velocity field, in addition to achieving a higher numerical accuracy and a significant reduction in the computational time.

The vorticity transport equations (3) are discretized in time using the explicit, second-order accurate Adams–Bashforth scheme. The discretized form of the vorticity transport equations (3) for the three vorticity components in the Cartesian co-ordinates can be written as

$$\frac{\xi^{n+1} - \xi^n}{\Delta t} + 1.5 f_1^n - 0.5 f_1^{n-1} = 0 \tag{10}$$

$$\frac{\eta^{n+1} - \eta^n}{\Delta t} + 1.5 f_2^n - 0.5 f_2^{n-1} = 0 \tag{11}$$

$$\frac{\varsigma^{n+1} - \varsigma^n}{\Delta t} + 1.5 f_3^n - 0.5 f_3^{n-1} = 0 \tag{12}$$

where

$$f_1 = \frac{\delta_y}{\Delta y}(v\xi) + \frac{\delta_z}{\Delta z}(w\xi) - \frac{\delta_y}{\Delta y}(\eta u) - \frac{\delta_z}{\Delta z}(\varsigma u) - \frac{1}{Re}\left(\frac{\delta^2}{\Delta x^2} + \frac{\delta^2}{\Delta y^2} + \frac{\delta^2}{\Delta z^2}\right)\xi$$

$$f_2 = \frac{\delta_x}{\Delta x}(u\eta) + \frac{\delta_z}{\Delta z}(w\eta) - \frac{\delta_x}{\Delta x}(\xi v) - \frac{\delta_z}{\Delta z}(\varsigma v) - \frac{1}{Re}\left(\frac{\delta^2}{\Delta x^2} + \frac{\delta^2}{\Delta y^2} + \frac{\delta^2}{\Delta z^2}\right)\eta$$

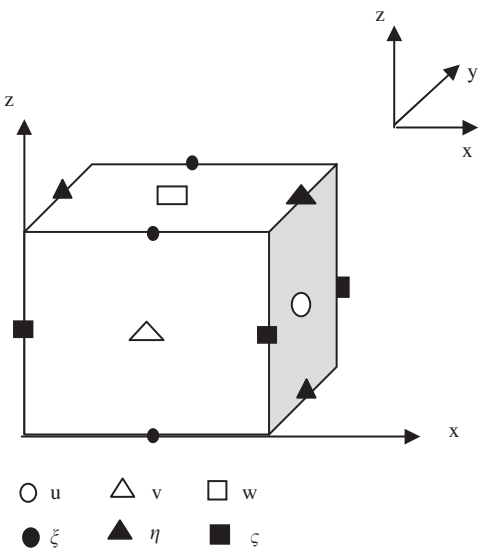

Figure 1. Three-dimensional staggered grid.

$$f_3 = \frac{\delta_x}{\Delta x}(u\varsigma) + \frac{\delta_y}{\Delta y}(v\varsigma) - \frac{\delta_x}{\Delta x}(\xi w) - \frac{\delta_y}{\Delta y}(\eta w) - \frac{1}{Re}\left(\frac{\delta^2}{\Delta x^2} + \frac{\delta^2}{\Delta y^2} + \frac{\delta^2}{\Delta z^2}\right)\varsigma$$

and δ_x, δ_y, δ_z are the first-order central difference operators, δ_x^2, δ_y^2, δ_z^2 are the second-order central difference operators. In order to ensure accuracy in the prediction of velocities and vorticities, a MAC staggered grid system as displayed in Figure 1 is used in the present numerical scheme. The final form of the discretized equations (8) and (10)–(12) for velocities and vorticities, respectively, are second-order accurate in time and space. The numerical stability conditions are satisfied by using the conservative form of the vorticity transport equations in the discretized form as expressed by Equations (10)–(12) and using a time step calculated based on the following numerical stability condition:

$$\left|\frac{u_{\max}\Delta t}{\Delta x}\right| \leqslant 1, \left|\frac{v_{\max}\Delta t}{\Delta y}\right| \leqslant 1, \left|\frac{w_{\max}\Delta t}{\Delta z}\right| \leqslant 1 \tag{13}$$

$$\frac{\Delta t}{Re}\left(\frac{1}{\Delta x^2} + \frac{1}{\Delta y^2} + \frac{1}{\Delta z^2}\right) \leqslant \frac{1}{2} \tag{14}$$

4. MODEL APPLICATION

Traditionally, the velocity and pressure are treated as the primitive variables while analyzing a viscous incompressible flow problem. That means the Navier–Stokes equations (2) and the

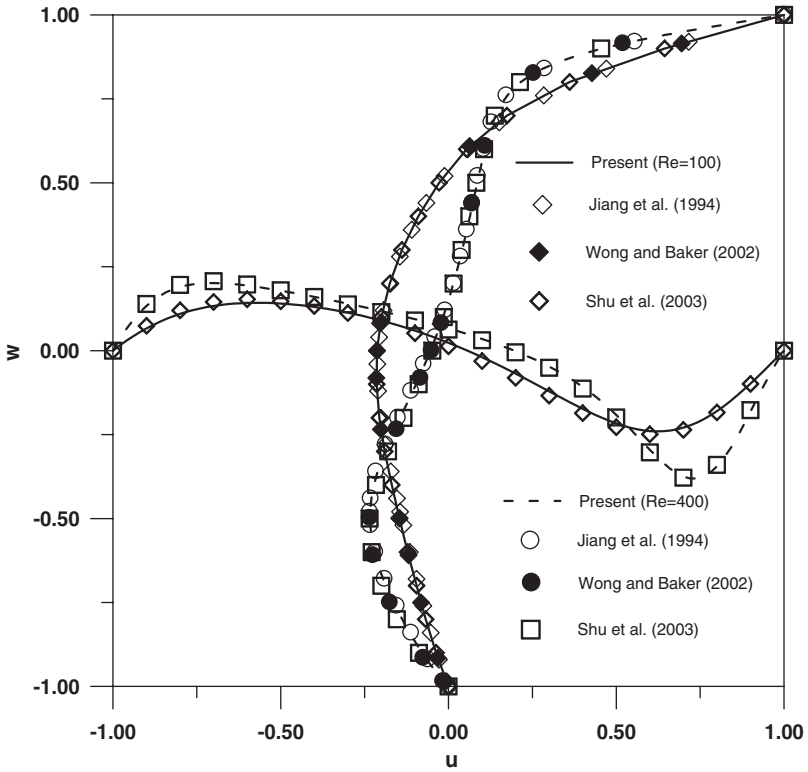

Figure 2. Velocity profiles for $Re = 100$ and 400 on vertical and horizontal centrelines.

continuity equation (1) should be taken into consideration simultaneously. However, while solving these two sets of equations, pressure and velocity are involved during the iterating process. However it is rather difficult to implicitly deal with the continuity equation because there is no pressure term in Equation (1). On the other hand, the velocity–vorticity formulation has no such problem because it is free from the pressure term. In the present model, the velocity Poisson equations are initially solved to get the velocity distribution. The vorticity boundary conditions are calculated using the vorticity definition for an initial guess of the wall vorticity boundary conditions.

The lid-driven cavity flow problem is always considered as a bench mark problem for testing any new numerical scheme. The present finite difference numerical procedure is validated by applying it to a cubical lid-driven cavity problem, in which the top wall is assumed to move parallel to the x-axis (refer Figure 1) with constant velocity of unity (dimensionless). The fluid in the cavity is assumed to be viscous and incompressible. In the present work, results were obtained for the lid-driven cavity flow for $Re = 100$ using a $51 \times 51 \times 51$ uniform mesh and for $Re = 400$, 1000 and 2000 using a uniform mesh of size $101 \times 101 \times 101$.

In the three-dimensional Navier–Stokes equations system, the intensity of the non-linearity, the diffusion and the convective effects are related with the magnitude of the Reynolds number. Therefore, fine meshes have to be used while solving high Reynolds number flows. Accurate

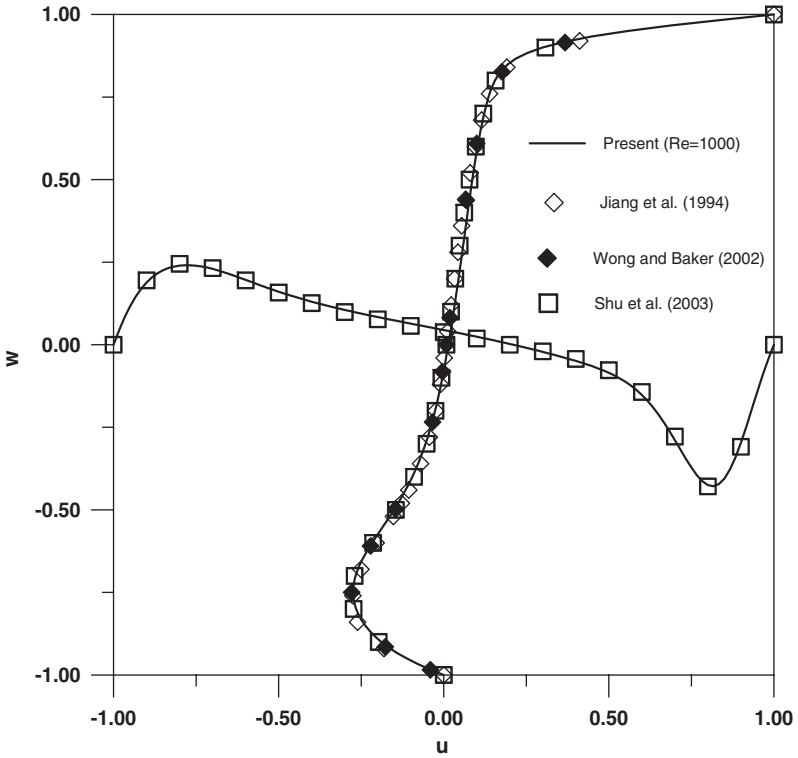

Figure 3. Velocity profiles for $Re = 1000$ on vertical and horizontal centrelines.

predictions for different Reynolds number flows can be obtained only by using an appropriate mesh. The results obtained are also strongly associated with the way in which the mesh size is adopted. We require to use a high-density mesh in the regions of steep gradients of the field variables, in order to capture the development of the boundary layer with increase in the Reynolds number. At low values of Reynolds number the diffusion plays a significant role in the formation of the flow field, however when the Reynolds number is increased to 100, the convection effects modify the diffusion process. In the present work the numerical results predicted for $Re = 100$, 400, 1000 and 2000 are discussed. All the computations have been carried out on a 1.5 GHz Pentium-IV personal computer with 256 Mb RAM.

The results obtained by the present numerical method for a 3D lid-driven cavity flow are presented in the form of velocity vectors and vorticity contours at the mid-planes along the principal axes of the cavity in order to understand the flow patterns at different Reynolds numbers. For the purpose of validation, the u velocity profile along the vertical central line (u–z plot) and the w velocity profile along the horizontal central line (x–w plot) of the cavity are compared with available results. Figures 2 and 3 show the u–z comparisons with the results of Jiang *et al.* [29], Wong and Baker [9] and Shu *et al.* [30] and x–w comparisons with the results of Shu *et al.* [30] for $Re = 100$, 400 and 1000. The results predicted by the present scheme are in close agreement with the results of the above authors for $Re = 100$,

Table I. Comparison of maximum negative u velocity.

	Present		Reference [29]		Reference [9]	
Re	z	u	z	u	z	u
100	0.46	−0.2163	0.48	−0.212	0.4592	−0.2154
400	0.26	−0.2334	0.26	−0.2341	0.2509	−0.2349
1000	0.12	−0.2671	0.12	−0.2754	0.125	−0.2792

Table II. u velocity along the vertical centreline of the 3D-driven cavity.

z location	$Re = 100$	$Re = 400$	$Re = 1000$	$Re = 2000$
0	0	0	0	0
0.04	−0.02928	−0.0645	−0.15736	−0.16252
0.08	−0.05430	−0.11576	−0.23687	−0.2429
0.1	−0.06578	−0.13817	−0.25743	−0.26394
0.12	−0.07675	−0.15886	−0.26714	−0.26501
0.14	−0.08740	−0.17779	−0.26615	−0.24457
0.16	−0.09780	−0.19471	−0.25535	−0.21002
0.2	−0.11815	−0.22071	−0.21285	−0.13603
0.22	−0.12816	−0.22882	−0.18648	−0.10671
0.24	−0.13809	−0.23313	−0.15988	−0.08372
0.26	−0.14789	−0.23343	−0.13468	−0.06607
0.3	−0.16687	−0.22212	−0.09161	−0.04199
0.32	−0.17587	−0.21108	−0.07413	−0.03363
0.36	−0.19227	−0.1809	−0.0463	−0.02111
0.4	−0.20548	−0.1443	−0.02574	−0.01183
0.42	−0.21047	−0.12518	−0.01738	−0.00786
0.44	−0.21414	−0.10619	−0.00997	−0.00413
0.46	−0.21632	−0.08772	−0.00328	−0.00055
0.5	−0.21561	−0.05334	0.00856	0.0065
0.52	−0.21247	−0.03767	0.01399	0.01011
0.56	−0.20017	−0.00952	0.02434	0.01777
0.58	−0.19092	0.00306	0.0294	0.02191
0.64	−0.15073	0.03599	0.04476	0.036
0.66	−0.13324	0.04573	0.05008	0.04133
0.68	−0.11369	0.05505	0.05558	0.04697
0.72	−0.06807	0.07288	0.06723	0.05918
0.76	−0.01206	0.09045	0.08011	0.07255
0.78	0.02111	0.09954	0.08716	0.07967
0.8	0.05888	0.10919	0.0947	0.08713
0.84	0.15361	0.13287	0.11205	0.10339
0.88	0.28593	0.17537	0.1349	0.12264
0.9	0.37125	0.21562	0.15264	0.13468
0.92	0.47149	0.28139	0.18367	0.15167
0.94	0.58704	0.3865	0.24776	0.18533
0.96	0.71653	0.54381	0.38323	0.27562
0.98	0.85624	0.75538	0.63626	0.52063
1	1	1	1	1

Table III. w velocity along the horizontal centreline of the 3D-driven cavity.

x location	$Re = 100$	$Re = 400$	$Re = 1000$	$Re = 2000$
0	0	0	0	0
0.04	0.06358	0.11371	0.16087	0.1792
0.06	0.08845	0.14992	0.20336	0.21512
0.08	0.10899	0.17454	0.2265	0.2297
0.1	0.12547	0.18978	0.23616	0.2293
0.12	0.13825	0.19794	0.23647	0.21742
0.14	0.14767	0.20103	0.23013	0.19818
0.18	0.15784	0.19788	0.2057	0.15434
0.2	0.15927	0.19351	0.19092	0.13496
0.24	0.15627	0.18176	0.16154	0.10471
0.26	0.15232	0.17493	0.14795	0.09328
0.3	0.14041	0.16006	0.12362	0.07556
0.32	0.13272	0.15216	0.11279	0.06852
0.38	0.10370	0.12677	0.08438	0.05162
0.42	0.07977	0.10826	0.06779	0.04242
0.48	0.03708	0.07738	0.04487	0.03007
0.52	0.00388	0.05411	0.03027	0.02216
0.54	−0.01419	0.04147	0.02305	0.01816
0.56	−0.03326	0.02803	0.01583	0.01405
0.6	−0.07418	−0.00185	0.00114	0.00528
0.62	−0.09585	−0.01872	−0.00644	0.00049
0.64	−0.11811	−0.03729	−0.01431	−0.00464
0.66	−0.14066	−0.05797	−0.02259	−0.01018
0.68	−0.16315	−0.08129	−0.0315	−0.0162
0.72	−0.20578	−0.1381	−0.05266	−0.02986
0.74	−0.22454	−0.1725	−0.06632	−0.03766
0.76	−0.24048	−0.2111	−0.0837	−0.04627
0.78	−0.25264	−0.2527	−0.10686	−0.056
0.82	−0.26169	−0.3346	−0.18149	−0.08235
0.84	−0.25687	−0.36537	−0.23736	−0.10387
0.86	−0.24502	−0.38096	−0.30346	−0.1384
0.88	−0.22595	−0.37533	−0.3694	−0.19475
0.9	−0.19991	−0.34516	−0.41506	−0.27727
0.92	−0.16756	−0.29166	−0.41534	−0.36774
0.94	−0.12997	−0.22098	−0.3548	−0.40986
0.96	−0.08851	−0.14255	−0.2435	−0.34083
0.98	−0.04468	−0.0663	−0.11416	−0.17465
1	0	0	0	0

400 and 1000. The comparison of the minimum u velocity with the results of Jiang *et al.* [29] and Wong and Baker [9] for $Re = 100$, 400 and 1000 as given in Table I shows the present numerical scheme could predict the flow results with acceptable numerical error. The minimum u velocity calculated by Wong and Baker [9] is 0.2154 for $Re = 100$, compared to 0.2163 computed by the present study, with an error of 0.42%. The values of u velocity along the z direction and values of w velocity along the x direction for selected nodal points are given in Tables II and III, respectively, for $Re = 100$, 400, 1000 and 2000. The efficiency of the present numerical scheme can be well appreciated by noting that the present results are obtained using entirely a different numerical scheme compared to Jiang *et al.* [29] who used

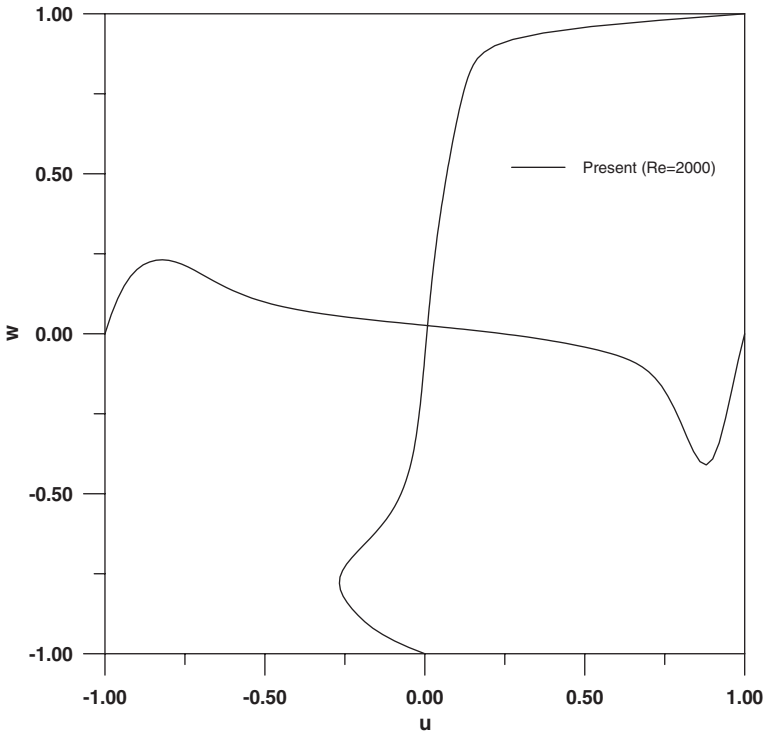

Figure 4. Velocity profiles for $Re = 2000$ on vertical and horizontal centrelines.

the least square finite element method and Wong and Baker [9] who obtained results using eight-node hexahedral finite elements on a non-staggered grid. Having validated the code up to $Re = 1000$, results are obtained for $Re = 2000$ using a uniform grid of size $101 \times 101 \times 101$. The u–z plot and x–w plot for $Re = 2000$ are shown in Figure 4. The increase in the Reynolds number value from 1000 to 2000 has resulted in further thinning of the boundary layer near the moving wall as observed in Figure 4 by the sharp velocity gradient. Also it develops a dip in the u–z velocity profile before reaching the minimum value.

The most important feature of 3D cavity flows is the end wall effect, which is not observed in the case of 2D cavity flows. The end wall effect produces different flow patterns resulting in the formation of eddies and vortices. This flow structure could be well understood by the velocity and vorticity contours projected on the mid-planes along the principal axes of the cavity. The velocity vectors projected on $y = 0.5$ plane for $Re = 100$, 400, 1000 and 2000 are shown in Figures 5(a), (b), (c) and (d), respectively. For $Re = 100$, the axis of the primary vortex starts at the right upper region of the cavity. The end wall effect causes the axis of the primary vortex to move towards the centre of the cavity with increase in Reynolds number as observed in the above figures. The span wise flow becomes more important at high Reynolds number for 3D cavity flows. The velocity vector plots on $x = 0.5$ plane shown in Figures 6(a)–(d) highlight the generation of secondary vortices at high Reynolds numbers. Initially two vortices are observed at the symmetric centre plane and the vortices start moving

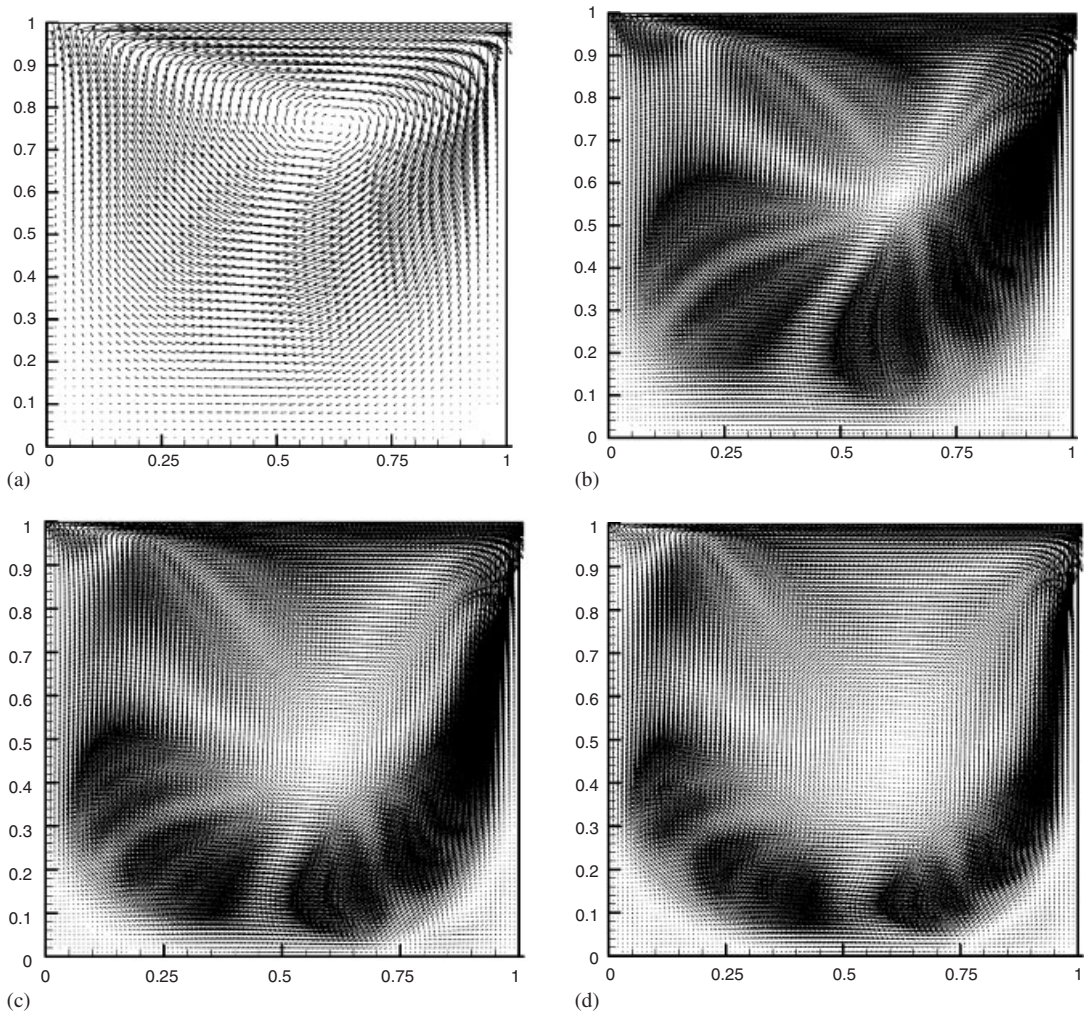

Figure 5. Velocity distribution at $y = 0.5$ plane. (a) $Re = 100$; (b) $Re = 400$; (c) $Re = 1000$; (d) $Re = 2000$.

towards the bottom as well as the end of the sidewalls with increase in Reynolds number. At $Re = 1000$, two recirculation cells also start appearing at the top ends of the sidewalls. The bottom vortices become strong at $Re = 2000$ as observed in Figure 6(d). The modifications of the flow fields at $x = 0.5$ plane for different Reynolds number is an important consequence of the three-dimensional effect. The velocity vectors on $z = 0.5$ plane, which is parallel to the moving lid are shown in Figures 7(a)–(d) for $Re = 100$–2000. As the top lid moves in the positive x direction, the fluid is expected to take the opposite direction for the return flow as shown in Figure 7(a) for $Re = 100$. With increase in Reynolds number, the smooth flow parallel to the x-axis is disturbed. Since the flow is already flowing span wise in the x–y

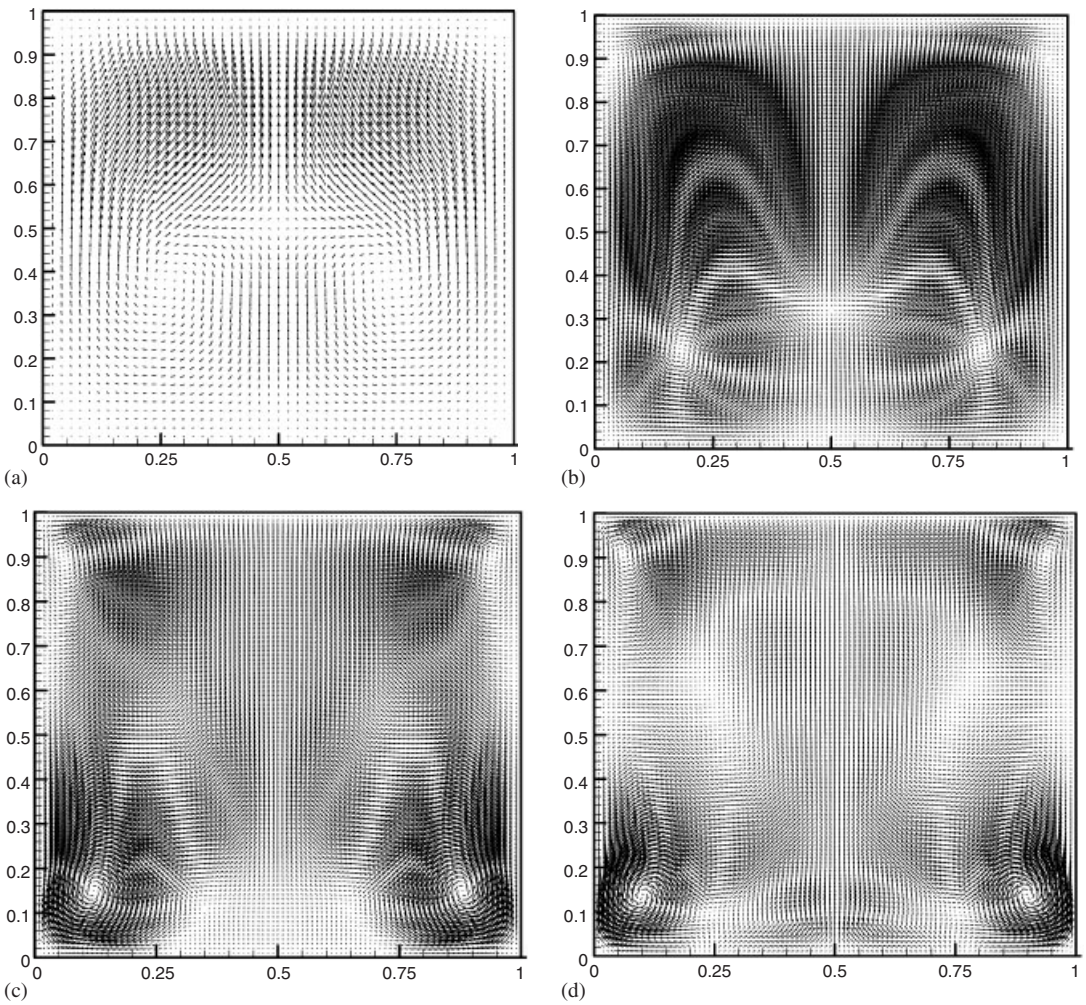

Figure 6. Velocity distribution at $x = 0.5$ plane. (a) $Re = 100$; (b) $Re = 400$; (c) $Re = 1000$; (d) $Re = 2000$.

plane, the effect of increase in Reynolds number is to make the flow in the z direction as well, thus making the flow fully three-dimensional. This results in the generation of two more symmetric vortices to the left of the original vortices. As the Reynolds number increases the initial vortices start diffusing at the centre of the cavity, with the secondary vortices start moving continuously towards the end walls. At $Re = 2000$, the secondary vortices also start merging along with the original vortices formed at the centre of the cavity. The velocity vectors projected on the centre planes of all the principal axes as illustrated in Figures 5–7, are in good qualitative agreement with the results of Wong and Baker [9] for $Re = 100$, 400 and 1000 and with the results of Jiang *et al.* [29], Nikfetrat and Hafez [31], Ho and Lin [32] and Ku *et al.* [33] for $Re = 100$ and 400. Similar comparisons of the velocity vectors on

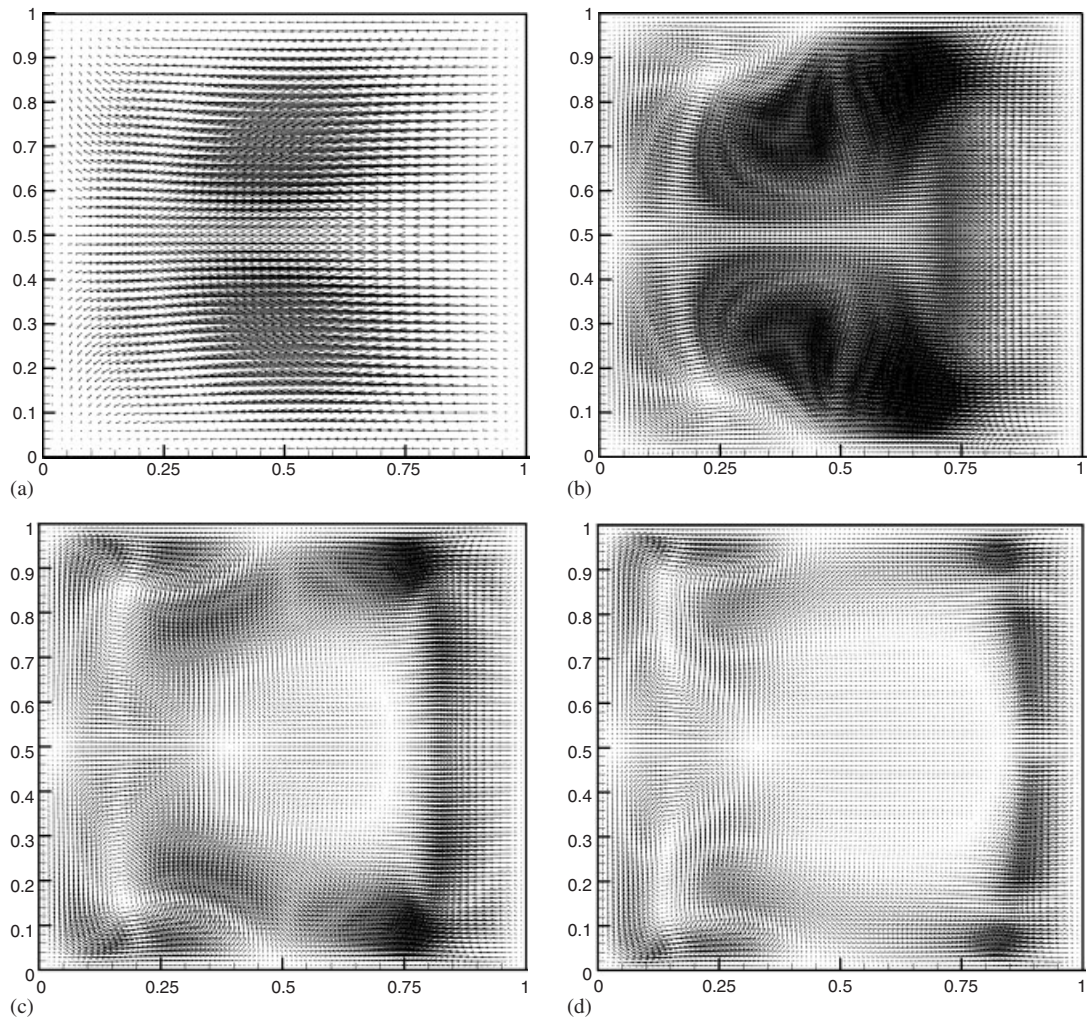

Figure 7. Velocity distribution at $z = 0.5$ plane. (a) $Re = 100$; (b) $Re = 400$; (c) $Re = 1000$; (d) $Re = 2000$.

$y = 0.5$ with the two-dimensional cavity flow results of Burggraff [34] and Ghia *et al.* [35] for $Re = 100$ and 400, indicates that the present model could predict the flow patterns in a 3D cubic cavity for a wide range of Reynolds numbers.

For obtaining the solution for velocities the continuity equation is satisfied as shown by Equation (9). Also the conservative forms of the vorticity transport equations (10)–(12) are solved to obtain the vorticity components. Hence the divergence-free solutions for the velocities and the vorticities are ensured. Since we use the vorticity definition to compute the boundary vorticity values, the solenoidal condition on the vorticity field is also satisfied as stated by Guj and Stella [12]. This fact can be verified by plotting the vorticity values at different planes of the cavity. The y direction vorticity contours at $y = 0.5$ plane for $Re = 100$,

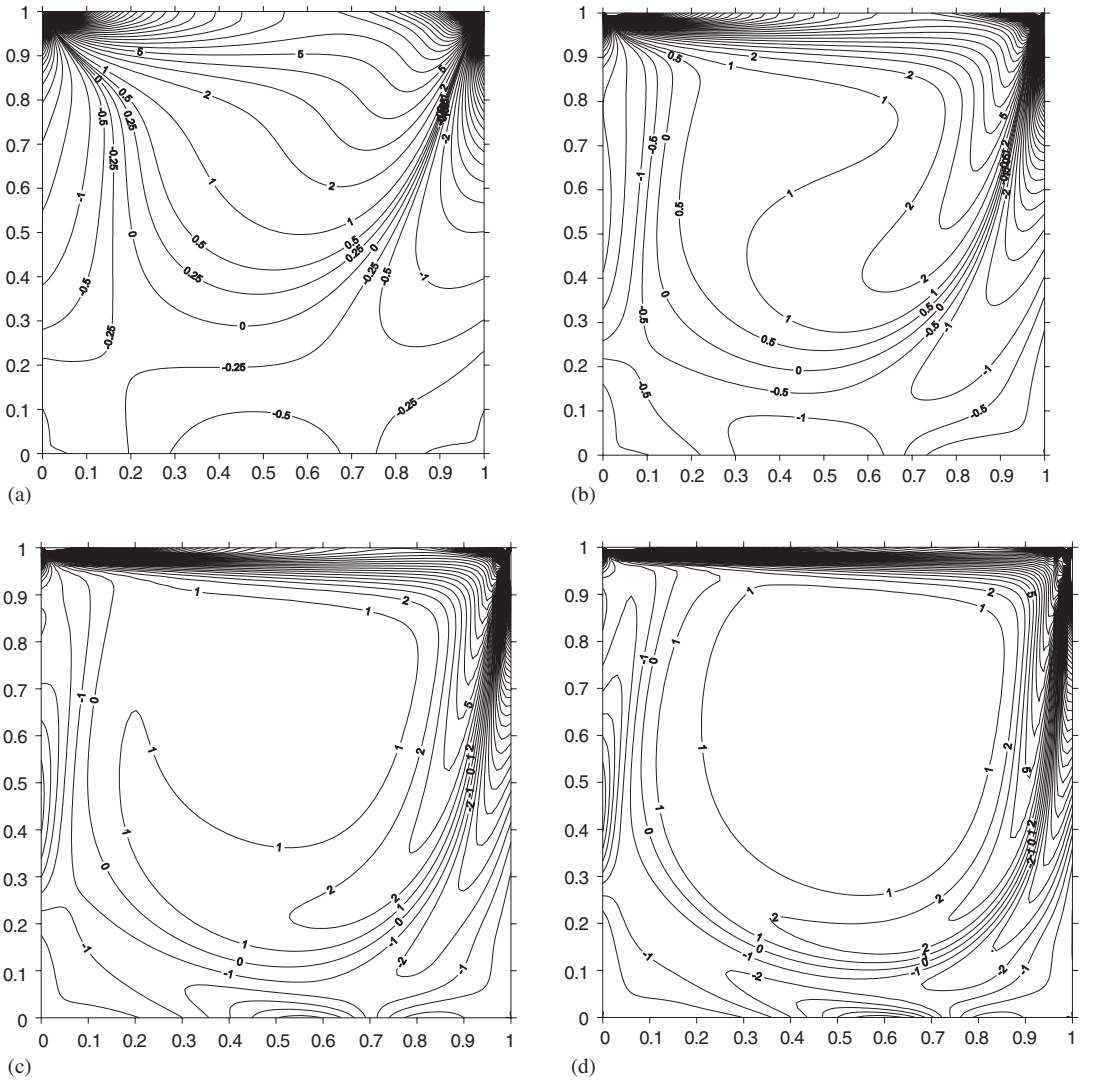

Figure 8. Vorticity (η) contour at $y = 0.5$ plane. (a) $Re = 100$; (b) $Re = 400$; (c) $Re = 1000$; (d) $Re = 2000$.

400, 1000 and 2000 are shown in Figures 8(a), (b), (c) and (d), respectively. The symmetry of the vorticity contours, which are observed in the case of Stokes flow, is disturbed for high Reynolds numbers as the inertial forces become dominating over the viscous forces. The direction of distortion will be counter-clockwise since the top lid is moving from left to right. Figure 8(a) clearly indicates these distortions for $Re = 100$. As the Reynolds number increases, the vorticity generated on the top wall and other boundary regions starts moving to other regions due to increase in the inertial forces as observed in Figures 8(b)–(d). These vortices

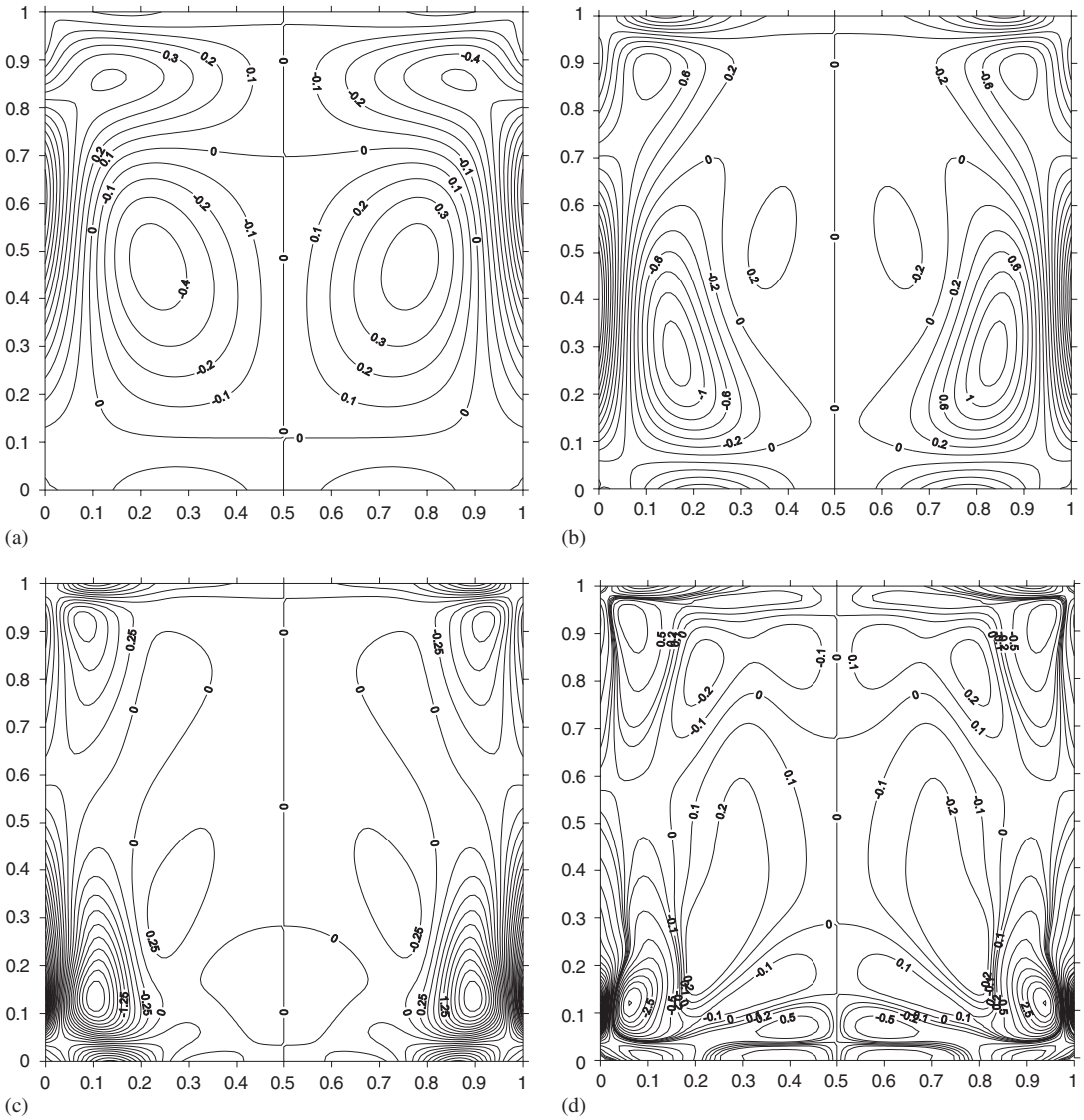

Figure 9. Vorticity (ξ) contour at $x = 0.5$ plane. (a) $Re = 100$; (b) $Re = 400$; (c) $Re = 1000$; (d) $Re = 2000$.

try to form a flow pattern similar to solid rotation if they get sufficient strength. This type of flow pattern could not be captured up to $Re = 1000$. When the Reynolds number increases to 2000, most of the vortices near the centre of the cavity have closed themselves, thus forming a flow pattern of solid rotation at the centre, as shown in Figure 8(d). In order to observe the 3D effect, the x direction vorticity contours at $x = 0.5$ plane for different Reynolds numbers are shown in Figures 9(a)–(d). At moderate Reynolds numbers, the secondary vortices are not ob-

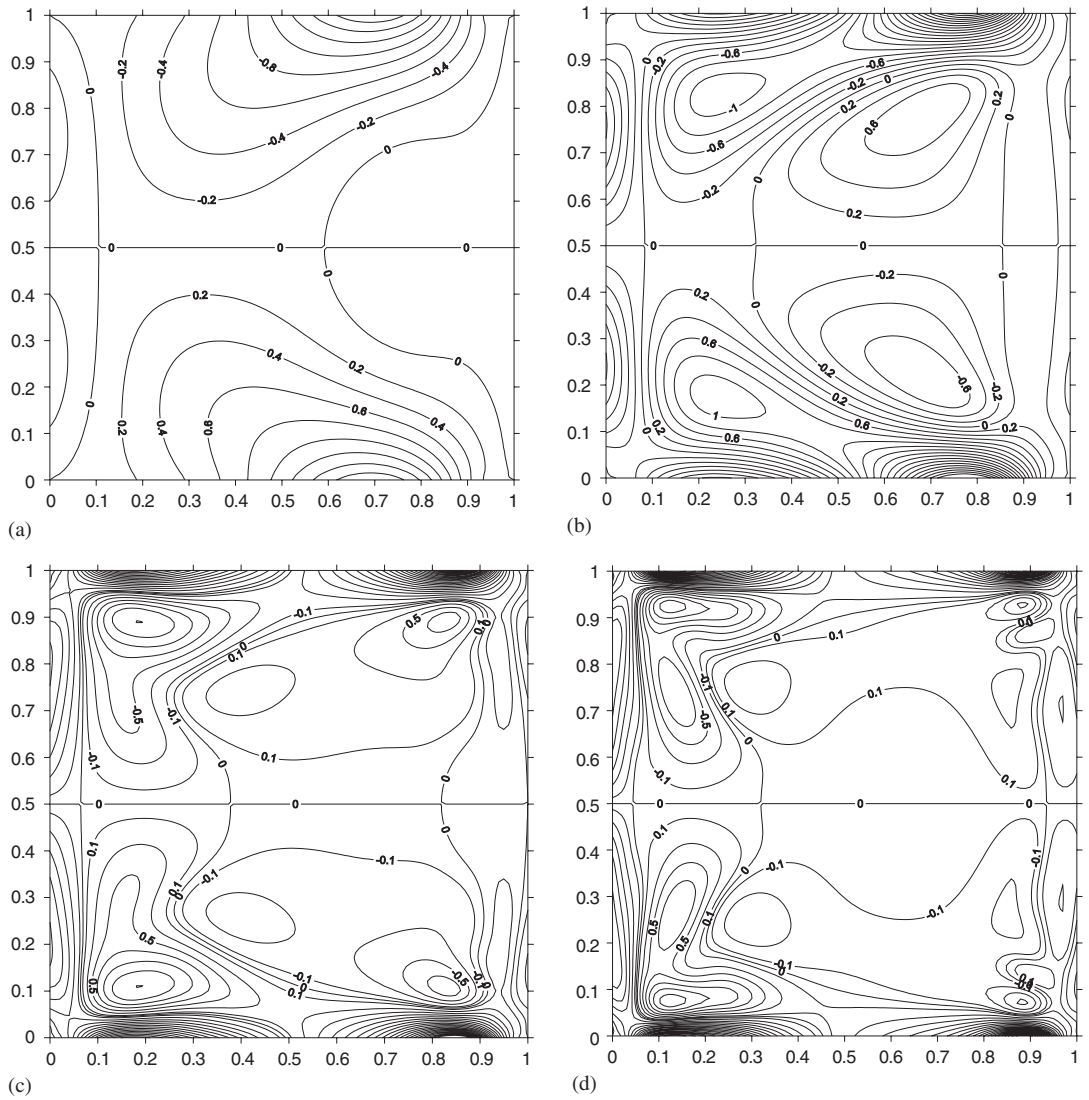

Figure 10. Vorticity (ζ) contour at $z = 0.5$ plane. (a) $Re = 100$; (b) $Re = 400$; (c) $Re = 1000$; (d) $Re = 2000$.

served. As the Reynolds number increases, these secondary vortices start moving towards the corners of the cavity due to the end wall effects. These trends are clearly depicted by the above figures with increase in Reynolds number. The approach of these secondary vortices to the extreme corners of the cavity are very clearly observed for $Re = 2000$ as shown in Figure 9(d). The z direction vorticity contours at $z = 0.5$ plane are shown in Figures 10(a)–(d). Initially for $Re = 100$, the vortex strength starts appearing only at the upper and bottom downstream regions of the x–y plane. As the Reynolds number increases, the flow takes place in

the z direction also, thus causing the generation of velocity gradients along the other sides of the x–y plane. This results in the formation of vortices originally closer to the initial vortices and these secondary vortices gain more strength and start moving towards the corners as the Reynolds number increases. These flow patterns can be clearly observed from the above figures. In general it is observed that the flow pattern becomes more complex as the Reynolds number increases above 1000.

5. CONCLUSIONS

A finite difference numerical solution procedure for solving three-dimensional Navier–Stokes equations in velocity–vorticity form is tested for a lid-driven cubical cavity flow. The simplified numerical procedure has enabled us the use of a very fine mesh of size $101 \times 101 \times 101$ for numerical predictions of cavity flow up to $Re = 2000$ on a Pentium-IV personal computer. The numerical results obtained for $Re = 100$, 400, 1000 for a typical cubic cavity flow are in good agreement with the results obtained by other numerical schemes. The use of a uniform fine mesh of size $101 \times 101 \times 101$ could predict the complex flow patterns when the Reynolds number is increased to 2000. When parallel computation is the order of the day, the present numerical scheme demonstrates that the finite difference method could be used efficiently for solving high Reynolds number flow problems in three dimensions using a personal computer.

ACKNOWLEDGEMENTS

We acknowledge the financial support from NSC, Taiwan, it is greatly appreciated.

REFERENCES

1. Glowinski R, Pironneau O. Finite element methods for Navier–Stokes equations. *Annual Review of Fluid Mechanics* 1992; **24**:167–204.
2. Fernandez G, Hafez M. Stable finite-element solution of the incompressible Navier–Stokes equations using linear interpolations for velocity and pressure. *Computer Methods in Applied Mechanics and Engineering* 2001; **191**:545–559.
3. Thomasset. *Implementation of Finite Element Methods for the Navier–Stokes Equations*. Springer: Berlin, 1981.
4. Young DL, Huang JL, Eldho TI. Simulation of laminar vortex shedding flow past cylinders using a coupled BEM and FEM model. *Computer Methods in Applied Mechanics and Engineering* 2001; **190**:5975–5998.
5. Young DL, Chang JT, Eldho TI. A coupled BEM and arbitrary Lagrangian–Eulerian FEM model for the solution of two-dimensional laminar flows in external flow fields. *International Journal for Numerical Methods in Engineering* 2001; **51**:1053–1077.
6. Elshabka AM, Chung TJ. Numerical solution of three-dimensional stream function vector components of vorticity transport equations. *Computer Methods in Applied Mechanics and Engineering* 1999; **170**:131–153.
7. Giese JH. Stream functions for three-dimensional flows. *Journal of Mathematical Physics* 1951; **30**(1):31–35.
8. Weinan E, Liu JG. Finite difference methods for 3D viscous incompressible flows in the vorticity-vector-potential formulation on nonstaggered grids. *Journal of Computational Physics* 1997; **138**:57–82.
9. Wong KL, Baker AJ. A 3D incompressible Navier–Stokes velocity–vorticity weak form finite element algorithm. *International Journal for Numerical Methods in Fluids* 2002; **38**:99–123.
10. Young DL, Yang SK, Eldho TI. Solution of the Navier–Stokes equations in velocity–vorticity form using a Eulerian–Lagrangian boundary element method. *International Journal for Numerical Methods in Fluids* 2000; **34**:627–650.
11. Young DL, Liu YH, Eldho TI. A combined BEM-FEM model for the velocity–vorticity formulation of the Navier–Stokes equations in three dimensions. *Engineering Analysis with Boundary Elements* 2000; **24**: 307–316.

12. Guj G, Stella F. A vorticity–velocity method for the numerical solution of 3D incompressible flows. *Journal of Computational Physics* 1993; **106**:286–298.
13. Wu XH, Wu JZ, Wu JM. Effective vorticity–velocity formulations for three-dimensional incompressible viscous flows. *Journal of Computational Physics* 1995; **122**:68–82.
14. Giannattasio P, Napolitano M. Optimal vorticity conditions for the node-centred finite-difference discretization of the second-order vorticity–velocity equations. *Journal of Computational Physics* 1996; **127**:208–217.
15. Clercx HJH. A spectral solver for the Navier–Stokes equations in the velocity–vorticity formulation for flows with two nonperiodic directions. *Journal of Computational Physics* 1997; **137**:186–211.
16. Trujillo J, Karniadakis GE. A penalty method for the vorticity–velocity formulation. *Journal of Computational Physics* 1999; **149**:32–58.
17. Goda K. A multistep technique with implicit difference schemes for calculating two- or three-dimensional cavity flows. *Journal of Computational Physics* 1979; **30**:76–95.
18. Guj G, Stella F. Numerical solutions of the high-Re recirculating flows in vorticity–velocity form. *International Journal for Numerical Methods in Fluids* 1988; **8**:405–416.
19. Daube O. Resolution of the 2D Navier–Stokes equations in velocity–vorticity form by means of an influence matrix technique. *Journal of Computational Physics* 1992; **103**:402–414.
20. Lo DC, Young DL. Two-dimensional incompressible flows by velocity–vorticity formulation and finite element method. *Chinese Journal of Mechanics* 2001; **17**(1):13–20.
21. Fasel H. Investigation of the stability of boundary layers by a finite-difference model of the Navier–Stokes equations. *Journal of Fluid Mechanics* 1976; **78**:355–383.
22. Orlandi P. Vorticity–velocity formulation for high Re flows. *Computers and Fluids* 1987; **15**:137–149.
23. Liu CH. Numerical solution of three-dimensional Navier–Stokes equations by a velocity–vorticity method. *International Journal for Numerical Methods in Fluids* 2001; **35**:533–557.
24. Napolitano M, Pascazio G. A numerical method for the vorticity–velocity Navier–Stokes equations in two and three dimensions. *Computer and Fluids* 1991; **19**:489–495.
25. Guevremont G, Habashi WG, Hafez MM. Finite element solution of the Navier–Stokes equations by a velocity–vorticity method. *International Journal for Numerical Methods in Fluids* 1990; **11**:661–675.
26. Mallinson G, de Vahl Davis G. The method of the false transient for the solution of coupled elliptic equations. *Journal of Computational Physics* 1973; **12**:435–461.
27. Napolitano M, Catalano LA. A multigrid solver for the vorticity–velocity Navier–Stokes equations. *International Journal for Numerical Methods in Fluids* 1991; **13**:49–59.
28. Batchelor GK. *Introduction to Fluid Dynamics*. Cambridge University Press: Cambridge, 1967.
29. Jiang BN, Lin TL, Povinelli LA. Large-scale computation of incompressible viscous flow by least-squares finite element method. *Computer Methods in Applied Mechanics and Engineering* 1994; **114**:213–231.
30. Shu C, Wang L, Chew YT. Numerical computation of three-dimensional incompressible Navier–Stokes equations in primitive variable form by DQ method. *International Journal for Numerical Methods in Fluids* 2003; **43**:345–368.
31. Nikfetrat K, Hafez M. Three dimensional viscous incompressible flow simulations using Helmholtz velocity decomposition. *Computational Fluid Dynamics Journal* 2002; **10**(4):439–445.
32. Ho CJ, Lin FH. Numerical simulation of three-dimensional incompressible flow by a new formulation. *International Journal for Numerical Methods in Fluids* 1996; **23**:1073–1084.
33. Ku HC, Hirsh RS, Taylor TD. A pseudospectral method for solution of the three-dimensional incompressible Navier–Stokes equations. *Journal of Computational Physics* 1987; **70**:439–462.
34. Burggraff OR. Analytic and numerical studies of structure of steady separated flows. *Journal of Fluid Mechanics* 1966; **24**:131–151.
35. Ghia U, Ghia KN, Shin CT. High-Re solutions for incompressible flow using the Navier–Stokes equations and a multigrid method. *Journal of Computational Physics* 1982; **48**:387–411.

